Grazing-incidence small-angle X-ray scattering technique for nanostructure determination of surfaces and interfaces of thin films

Yoshiyasu Ito*

1. Introduction

Recently, nanotechnology has made striking advances in the fabrications of nano-electronic and nano-magnetic devices. Some of the new nanostructures are nano-particles, nanodots, nanowires, nanotubes, etc. Most of these nanostructures are often fabricated on the surface and/or at the interfaces of a thin film, and the nano-structures in many cases exhibit anisotropies along the normal and the parallel directions of the surface and interfaces.

Small-angle X-ray scattering (SAXS) technique has widely been used for the determination of structures of materials in the micrometer and nanometer ranges by measuring scattering intensities at scattered angles 2θ close to 0°. The types of structures can be determined including average particle sizes, shapes, distributions, surface to volume ratio, etc.

In order to determine anisotropic micro and nano-structures along both the normal and parallel directions in a thin film, the use of grazing incidence X-ray technique together with the small-angle scattering technique, namely grazing incidence small-angle X-ray scattering (GI-SAXS), is required.

2. Instrumentation for GI-SAXS

For the SAXS characterization of density fluctuations in a liquid or bulk sample, the transmission geometry (i.e., T-SAXS) is often used. However, T-SAXS intensities caused by density fluctuations in a thin film deposited on a thick substrate are extremely weak, if not undetectable, because X-rays are absorbed and cannot transmit through the thick substrate. On the other hand, in GI-SAXS, scattered X-rays are not absorbed by the substrate. In addition, GI-SAXS has an advantage of use a large scattering volume (total volume of scatters contributing to SAXS). The scattering volume in GI-SAXS is $1/\sin\theta$ times larger than that in T-SAXS.

In a GI-SAXS experiment, X-ray scattering data are collected along both the surface normal (Q_Z in Fig. 1) and the parallel (Q_Y in Fig. 1) directions of a thin film. The GI-SAXS curves measured along the Q_Z and Q_Y directions are used to determine the anisotropic nano-structures of the surfaces and interfaces in the film.

2.1. X-ray source and optics for GI-SAXS

The spot size and the divergent angles of the incident X-ray beam are critical for the performance of a GI-SAXS experiment. GI-SAXS intensities are collected along both the Q_Y and the Q_Z directions (see Fig. 1), and the grazing angle between the incident X-ray beam and the film surface is normally less than 1°. Therefore, micro-focused, well-collimated, and high-fluxed X-ray beam is necessary for a GI-SAXS experiment. In about ten years ago, such an ideal X-ray beam can only be obtained from a synchrotron radiation source, and most of GI-SAXS experiments have been performed at synchrotron radiation facilities.[1],[2] However, recent advances in the development of micro-focused X-ray generators and Confocal Max-Flux (CMF) mirror optics make possible to conduct in-house GI-SAXS experiments.[3] CMF mirror optics have also used in many in-house X-ray diffraction (XRD) experiments.

Two types of CMF mirrors have recently been developed. One is a focus-focus type CMF mirror with a combination of two elliptical mirrors to provide high X-ray flux (see top of Fig. 2). The focus-focus type CMF

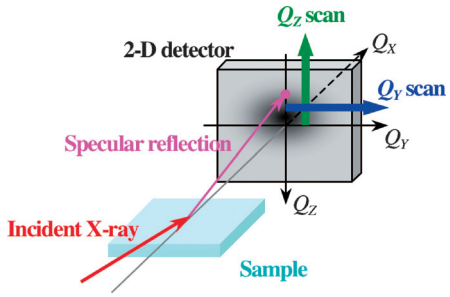

Fig. 1. Schematic diagram for GI-SAXS.

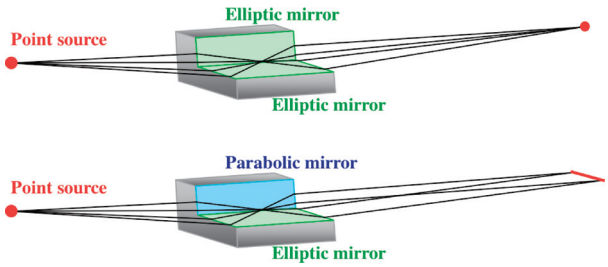

Fig. 2. Confocal Mux-Flux mirrors: top, focus-focus type CMF mirror (used in a NANO-Viewer); bottom, focus-parallel type CMF mirror (used in a SuperLab).

* Technology & Product Development Division, Rigaku Corporation.

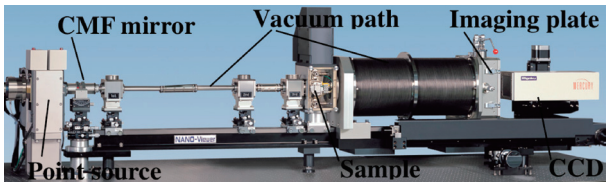

Fig. 3. A Rigaku NANO-Viewer for SAXS.

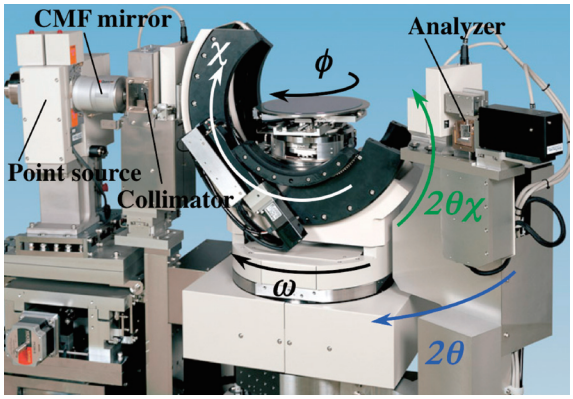

Fig. 4. A Rigaku SuperLab, a high-resolution X-ray diffractometor.

mirror has been equipped with X-ray systems used for SAXS (e.g., the Rigaku NANO-Viewer in Fig. 3) and single-crystal structural analysis, etc. The other is a focus-parallel type CMF mirror with a combination of an elliptical and a parabolic mirrors (see bottom of Fig. 1), and the focus-parallel mirror together with a crystal monochromator is used for GI-SAXS (see the Rigaku Super Lab system in Fig. 4) and high-resolution X-ray measurements such as high-resolution in-plane XRD, etc.

2.2. Detection of GI-SAXS

GI-SAXS data can be collected very rapidly using a two-dimensional (2D) detector. Since GI-SAXS intensities measured along both the Q_Y and the Q_Z directions can be recorded simultaneously by a 2D detector, GI-SAXS has the advantages for easy characterization of anisotropic nanostructures and for a dynamical study of phase transition in a thin film. However, GI-SAXS with a 2D detector also has a disadvantage that a 2D detector detects not scattering just by nanostructures but also by air in the X-ray beam path. In order to minimize air scattering, a vacuum or helium path can be used. Therefore, most of the SAXS system employed a 2D detector is specially designed for the use of helium or vacuum path. 2D detectors equipped with either an imaging plate (IP) or a charge-coupled device (CCD) camera are widely used in X-ray analysis for many years. A new pixel-array 2D detector operating in the single-photon counting mode, namely PILATUS 100 K, has recently been developed. PILATUS has a wide dynamic range, short read-out time, and high counting rate compared to those of IP and CCD detectors.

If GI-SAXS intensities are collected by a conventional zero-dimensional detector, such as a scintillation detector, an X-ray diffractometer has to be able to collect data along the Q_Y direction (2θ in Fig. 3) as well as the Q_Z direction (2θ in Fig. 3). Recently, grazing incidence X-ray diffraction (in-plane XRD measured along the Q_Y direction) has attracted a great deal attention and played important roles for characterizing crystal structures of ultra thin films with thickness down to a few nanometers. Therefore, most modern thin-film diffractometers are equipped with scanning axes along both the Q_Y and the Q_Z directions. Scan-based GI-SAXS measurements require a considerable long time to collect SAXS intensities along both the Q_Y and the Q_Z directions. However, scan-based GI-SAXS can effectively reduce air scattering by using two narrow slits of about 0.2 mm in width, and a vacuum or helium path is not required.

3. Scattering cross section based on DWBA method

For the transmission geometry, scattering cross section is calculated by plane-wave Born approximation method. In grazing incidence geometry, however, scattering cross section is calculated by distorted-wave Born approximation (DWBA) method to account for both reflections and transmissions (or refractions) at the film surface and interfaces.[4],[5]

3.1. Distorted waves in a thin film

Distorted waves in a thin film are briefly discussed. A refractive index of a substance for X-ray wavelength is slightly smaller than 1.0, and total reflection occur when a film surface is impinged by an X-ray beam with an angle equal to or smaller than the critical angle for total reflection of the substance. The critical angle for total reflection of a substance depends on its refractive index, and the values of the critical angle for total reflection vary from 0.1° to 0.5° for most substances. If an X-ray beam is impinged onto the surface of a film at a grazing angle, an X-ray wave field inside the film is developed by both reflections and refractions at the film interfaces. The X-ray wave field, which is a distorted-wave field, can be calculated by the Fresnel's formula.[6] X-ray wave field $\psi(\theta, \boldsymbol{X}, Z_j)$ in the j^{th} layer of a film (see Fig. 5) at the $(\boldsymbol{X}, Z_j)$ position can be written as follows:

$$\psi_j(\theta, \boldsymbol{X}, Z_j) = T_j(e^{ik_0\alpha_j Z_j} + R_j\varphi_j^2 e^{-ik_0\alpha_j Z_j})e^{i\boldsymbol{k}_0\cdot\boldsymbol{X}} \quad (1)$$

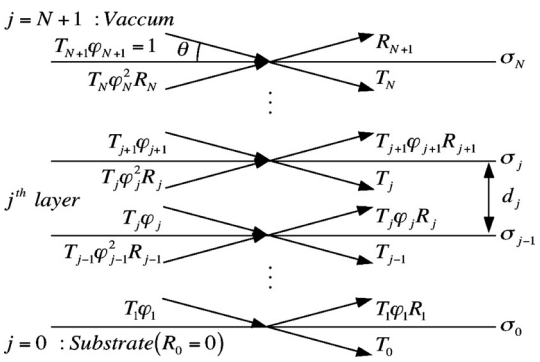

Fig. 5. Transmitted and reflected waves in a n-layer film.

where $\boldsymbol{k}_0$ is wave vector of the incident X-ray beam, θ angle of incidence, α_j, φ_j, T_j, and R_j are defined as follows:

$$\begin{aligned}
&\alpha_j = \sqrt{n_j^2 - \cos^2\theta}\ , \quad \varphi_j = e^{ik_0\alpha_j d_j} \\
&\gamma_j = \frac{\alpha_j - \alpha_{j-1}}{\alpha_j + \alpha_{j-1}} e^{-2k_0^2\sigma_{j-1}^2\alpha_j\alpha_{j-1}}, \quad \tau_j = \frac{2\alpha_{j-1}}{\alpha_j + \alpha_{j-1}}\ , \\
&t_j = \frac{1-\gamma_j R_j}{\tau_j} \\
&R_j = \frac{R_{j-1}\varphi_{j-1}^2 + \gamma_j}{R_{j-1}\varphi_{j-1}^2\gamma_j + 1}, \quad T_j = \prod_{l=j+1}^{N+1} t_l\varphi_l
\end{aligned} \tag{2}$$

where n_j, d_j, and σ_j are refractive index, thickness and roughness of the j^{th} layer, respectively, and these parameters can be determined by analyzing X-ray reflectivity $|R_{N+1}|^2$ data. The first term in Eq. (1) is for the transmitted wave and the second term for the reflected wave. The scatted wave can be represented by a time reversal state of the incoming wave. Therefore, the scatted wave field $\tilde{\psi}_j(\tilde{\theta}, \boldsymbol{X}, Z_j)$ in the j^{th} layer at the ($\boldsymbol{X}$, Z_j) position with an exit angle $\tilde{\theta}$ can be written the same way as Eq. (1) by using time reversal state, $\tilde{\alpha}_j^*$, $\tilde{\varphi}_j^*$, $\tilde{T}_j^*$, and $\tilde{R}_j^*$:

$$\tilde{\psi}_j(\tilde{\theta}, \boldsymbol{X}, Z_j) = \tilde{T}_j^*(e^{-ik\tilde{\alpha}_j^* Z_j} + \tilde{R}_j^*\tilde{\varphi}_j^{*2} e^{ik\tilde{\alpha}_j^* Z_j})e^{i\boldsymbol{k}\cdot\boldsymbol{X}} \tag{3}$$

$$\begin{aligned}
&\tilde{\alpha}_j^* = \sqrt{n_j^{*2} - \cos^2\tilde{\theta}}\ , \quad \tilde{\varphi}_j^* = e^{ik\,\tilde{\alpha}_j^* d} \\
&\tilde{\gamma}_j^* = \frac{\tilde{\alpha}_j^* - \tilde{\alpha}_{j-1}^*}{\tilde{\alpha}_j^* + \tilde{\alpha}_{j-1}^*} e^{-2k^2\sigma_{j-1}^2\tilde{\alpha}_j^*\tilde{\alpha}_{j-1}^*}, \quad \tilde{\tau}_j^* = \frac{2\tilde{\alpha}_{j-1}^*}{\tilde{\alpha}_j^* + \tilde{\alpha}_{j-1}^*} \\
&\tilde{t}_j^* = \frac{1-\tilde{\gamma}_j^*\tilde{R}_j^*}{\tilde{\tau}_j^*} \\
&\tilde{R}_j^* = \frac{\tilde{R}_{j-1}^*\tilde{\varphi}_{j-1}^{*2} + \tilde{\gamma}_j^*}{\tilde{R}_{j-1}^*\tilde{\varphi}_{j-1}^{*2}\tilde{\gamma}_j^* + 1}, \quad \tilde{T}_j^* = \prod_{i=j+1}^{N+1} \tilde{t}_j^*\tilde{\varphi}_j^*
\end{aligned} \tag{4}$$

The scattering cross section can be calculated by a transition from the initial state (Eq. (1)) to the scattered state (Eq. (2)).

3.2. Nanostructures on the surface of a substrate

If the scatters are dispersed on the surface of a substrate ($N=0$), the incoming wave and the scattered wave ($j=1$) can be written as:

$$\psi_1(\theta, \boldsymbol{X}, Z_1) = (e^{ik_0\alpha_1 Z_1} + R_1 e^{-ik_0\alpha_1 Z_1})e^{i\boldsymbol{k}_0\cdot\boldsymbol{X}} \tag{5}$$

$$\tilde{\psi}_1(\tilde{\theta}, \boldsymbol{X}, Z_1) = (e^{-ik\tilde{\alpha}_1^* Z_1} + \tilde{R}_1^* e^{ik\tilde{\alpha}_1^* Z_1})e^{i\boldsymbol{k}\cdot\boldsymbol{X}} \tag{6}$$

If the scatters are distributed randomly on the surface, the scattering cross section can be written as follows:

$$\begin{aligned}
\frac{d\sigma}{d\Omega} &= \left|\frac{\langle\tilde{\psi}_1|V(\boldsymbol{r})|\psi_1\rangle}{4\pi}\right|^2 = \left|\frac{1}{4\pi}\int_{\text{Surface}} \tilde{\psi}_1^* V(\boldsymbol{r})\psi_1 dv\right|^2 \\
&\approx N_1\left|\frac{1}{4\pi}\int_{\text{Scatter}} \tilde{\psi}_1^* V(\boldsymbol{r})\psi_1 dv\right|^2 = \frac{N_1}{16\pi^2}\begin{vmatrix} F(\boldsymbol{Q}_1) \\ +R_1F(\boldsymbol{Q}_2) \\ +\tilde{R}_1F(\boldsymbol{Q}_3) \\ +R_1\tilde{R}_1F(\boldsymbol{Q}_4)\end{vmatrix}^2
\end{aligned} \tag{7}$$

$$F(\boldsymbol{Q}) = \int_{\text{Scatter}} V(\boldsymbol{r})e^{-i\boldsymbol{Q}\cdot\boldsymbol{r}} dv$$

$$V(\boldsymbol{r}) = -r_e N_A\left(\frac{f_s + f_s'}{M_s} - \frac{f_m + f_m'}{M_m}\right) \tag{8}$$

where $V(\boldsymbol{r})$ is the scattering potential calculated by the difference in electron number densities between a scatter "s" and the matrix "m" of the film, r_e classical electron radius, N_A Avogadro number, M atomic weight, f atomic scattering factor, f' real part of anomalous scattering factor, $F(\boldsymbol{Q})$ form factor of the scatters, N_1 number of the scatters. The form factor $F(\boldsymbol{Q})$ contains information on the size and the shape of the scatters. The form factor is the scattering amplitude calculated by the plane-wave Born approximation. As shown in Eq. (7), there are a total of four scattering processes: (1) from a transmitted incoming wave to a transmitted scattered wave, (2) from a transmitted incoming wave to a reflected scattered wave, (3) from a reflected incoming wave to a transmitted scattered wave, (4) from a reflected incoming wave to a reflected scattered wave. Therefore, there are four scattering vectors in each scattering process. The four scattering vectors to the $\boldsymbol{X}$ direction $Q_X=(Q_X, Q_Y)$ are equal. The four scattering vectors can be written as:

$$\begin{aligned}
&Q_X = (\boldsymbol{k} - \boldsymbol{k}_0)\cdot\boldsymbol{e}_X \\
&Q_{1,Z} = -Q_{4,Z} = -k_0(\tilde{\alpha}_1 + \alpha_1) \\
&Q_{2,Z} = -Q_{3,Z} = -k_0(\tilde{\alpha}_1 - \alpha_1)
\end{aligned} \tag{9}$$

In addition, following the coordinate system shown in Fig. 1, the Q_X and Q_Y components can be written as:

$$\begin{aligned}
&Q_X = k_0(\cos\tilde{\theta}\cos 2\theta - \cos\theta) \\
&Q_Y = k_0\cos\tilde{\theta}\sin 2\theta
\end{aligned} \tag{10}$$

where 2θ is the scattering angle along the in-plane direction.

3.3. Nanostructures in a thin film

If the scatters vary in a single-layer film ($N=1$), the incoming wave and the scattered wave ($j=1$) can be written as follows:

$$\psi_1(\theta, \boldsymbol{X}, Z_1) = T_1(e^{ik_0\alpha_1 Z_1} + R_1\varphi_1^2 e^{-ik_0\alpha_1 Z_1})e^{i\boldsymbol{k}_0\cdot\boldsymbol{X}} \tag{11}$$

$$\tilde{\psi}_1(\tilde{\theta}, \boldsymbol{X}, Z_1) = \tilde{T}_1^*(e^{-ik\tilde{\alpha}_1^* Z_1} + \tilde{R}_1^*\tilde{\varphi}_1^{*2} e^{ik\tilde{\alpha}_1^* Z_1})e^{i\boldsymbol{k}\cdot\boldsymbol{X}} \tag{12}$$

If the scatters are distributed randomly in the film and the oscillated thickness fringes are ignored, the scattering cross section can be written as:

$$\frac{d\sigma}{d\Omega} \approx \frac{\rho_Z}{16\pi^2}\left|\tilde{T}_1 T_1\right|^2 \times \left\{ \begin{array}{l} \left|F(\boldsymbol{Q}_1)\right|^2 \dfrac{1-e^{-2k_0\,\mathrm{Im}(\tilde{\alpha}_1+\alpha_1)d_1}}{2k_0\,\mathrm{Im}(\tilde{\alpha}_1+\alpha_1)} \\ +\left|F(\boldsymbol{Q}_2)\right|^2\left|R_1\varphi_1^2\right| \dfrac{1-e^{-2k_0\,\mathrm{Im}(\tilde{\alpha}_1-\alpha_1)d_1}}{2k_0\,\mathrm{Im}(\tilde{\alpha}_1-\alpha_1)} \\ +\left|F(\boldsymbol{Q}_3)\right|^2\left|\tilde{R}_1\tilde{\varphi}_1^2\right| \dfrac{1-e^{-2k_0\,\mathrm{Im}(-\tilde{\alpha}_1+\alpha_1)d_1}}{2k_0\,\mathrm{Im}(-\tilde{\alpha}_1+\alpha_1)} \\ +\left|F(\boldsymbol{Q}_4)\right|^2\left|R_1\varphi_1^2\tilde{R}_1\tilde{\varphi}_1^2\right| \dfrac{e^{2k_0\,\mathrm{Im}(\tilde{\alpha}_1+\alpha_1)d_1}-1}{2k_0\,\mathrm{Im}(\tilde{\alpha}_1+\alpha_1)} \end{array} \right\} \quad (13)$$

where ρ_Z is the number of scatters per unit of depth, and Im(x) the imaginary part of a complex number x.

3.4. Form factor $F(Q)$

In a GI-SAXS analysis, the spatial distribution of scattering potential, $V(\boldsymbol{r})$, is used to mathematically represent the shape and the size of a scatter. If the form factor can be directly obtained from observed GI-SAXS curves, $V(\boldsymbol{r})$ can then be calculated by inverse Fourier transform of the form factor, $F(\boldsymbol{Q})$. However, it is not possible to obtain the form factor directly from the GI-SAXS curves, and only the square of the absolute value of the form factor can be obtained. This means the size and the shape of a scatter cannot be determined directly from the GI-SAXS curves. Therefore, the form factor is calculated based on a shape model with suitable parameters, and the parameters are optimized by matching the calculated to the observed GI-SAXS curves. Form factors for various shapes have been reported.[7] The form factor for the spherical shape (V=const.) with a radius R is given below:

$$\begin{aligned} F(\boldsymbol{Q},R) &= \int_0^R\int_0^\pi\int_0^{2\pi} Ve^{-iQr\cos\theta}r^2\sin\theta\, dr d\theta d\varphi \\ &= \frac{4\pi V}{Q^3}\{\sin(QR)-QR\cos(QR)\} \end{aligned} \quad (14)$$

For the spherical model, radius R is the only parameter needed to be optimized.

3.5. Size distribution of nanostructure

Scatters normally have large size distributions except in some proteins. The SAXS technique cannot be used to count the number of the scatters for each size, unlike the electron microscope technique. This is because an observed SAXS curve is the sum of SAXS curves for various sizes of the scatters. Therefore, the size distribution for the scatters is also calculated based on a selected distribution function with suitable parameters, such as the Γ-distribution and the Lognormal distribution functions. These distribution functions have a range from 0 to $+\infty$. On the other hand, the well-known Gauss and Lorenz distribution functions have a range from $-\infty$ to $+\infty$. Because the size of a scatter should be a positive numeral, the Gauss and Lorenz functions are not suitable. In this paper, the Γ-distribution function shown below is used to determine the scatter size distribution:

$$P(x;x_0,\Delta x) = \frac{1}{\Gamma(x_0^2/\Delta x^2)}\left(\frac{x_0}{\Delta x^2}\right)^{x_0^2/\Delta x^2} x^{-1+\frac{x_0^2}{\Delta x^2}} e^{-\frac{x_0}{\Delta x^2}x} \quad (15)$$

where x_0 is the average size, Δx the standard deviation of the distribution, and $\Gamma(x)$ the Γ-function. If the scatters have size distributions, the scattering cross section can be calculated as follows:

$$\frac{d\sigma}{d\Omega}(\boldsymbol{Q};x_0,\Delta x) = \int_0^\infty \frac{d\sigma}{d\Omega}(\boldsymbol{Q},x)P(x;x_0,\Delta x)dx \quad (16)$$

The x_0, Δx and other shape parameters of the scatters are simultaneously optimized.

4. GI-SAXS applications

4.1. Anisotropic shape of nanometer-sized pores in a porous low-k film

Low-k dielectric films are used as interlayer insulators in ultrahigh density integrated circuits in order to avoid a delay of signal propagation and cross talks. It was reported that the dielectric constant of a film can be reduced by introducing pores into the film. However, the introduction of such pores changes the physical property of the film, such as hardness, especially when larger pores are introduced. The structure of the pores and their size distributions are closely related to the properties of the porous thin film.

A GI-SAXS measurement of the porous structure was performed using a Rigaku SuperLab diffractometer (Fig. 3) equipped with a rotating anode X-ray generator operated at 40 kV and 30 mA, and Cu Kα (λ=0.154178 nm) radiation was used, using an incidence angle of 0.2°. GI-SAXS curves measured along the Q_Y and Q_Z directions were collected by scanning the 2θ and $2\theta\chi$ axes, respectively. Refractive index, film thickness and interface roughness, parameters for DWBA method, were estimated from the previously measured X-ray reflectivity data.

In the GI-SAXS analysis, Eq. (13) is used for the scattering cross section of the nanopores assuming the pores are distributed randomly in the film. Ellipsoidal shape with size anisotropy along the Q_Z direction for the pores was used. The form factor for an ellipsoidal shape pore can be written as:

$$\begin{aligned} F(\boldsymbol{Q};D,D_Z) &= \frac{4\pi VD_Z}{Q'^3D} \\ &\times\left\{\sin\left(\frac{Q'D}{2}\right)-\frac{Q'D}{2}\cos\left(\frac{Q'D}{2}\right)\right\} \\ Q' &= \sqrt{Q_X^2+Q_Y^2+(D_Z/D)^2Q_Z^2} \end{aligned} \quad (17)$$

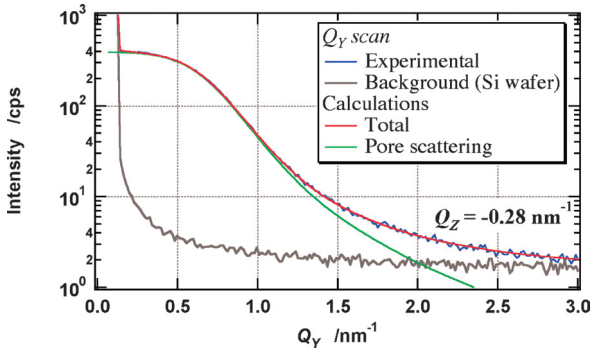

Fig. 6. GI-SAXS curves measured along the Q_Y direction for the porous low-*k* film.

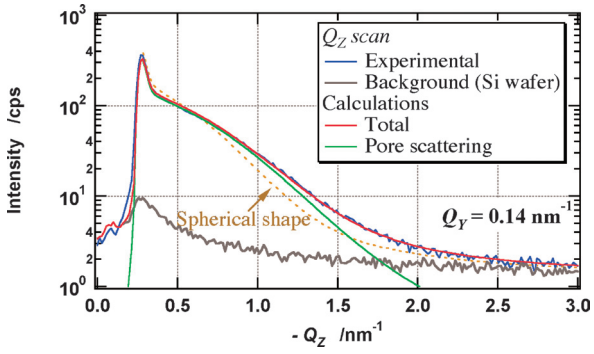

Fig. 7. GI-SAXS curves measure along the Q_Z direction for the porous low-*k* film.

where D and D_Z are diameters of a pore in the surface parallel and normal directions, respectively. The observed and calculated GI-SAXS curves in the Q_Y direction (surface parallel) are shown in Fig. 6, and those in the Q_Z direction (surface normal) are show in Fig. (7). Q_Z in Figs. 6 and 7 is $-k_0(\tilde{\alpha}_2+\alpha_2)=-k_0(\sin\tilde{\theta}+\sin\theta)$. Final pore-size distributions in the directions of surface parallel and normal obtained by using the optimized parameters are shown in Fig. 8. For comparison, the GI-SAXS curve calculated by the spherical shape with a diameter of D is also shown in Fig. 7. If each of the pores is assumed to have a spherical shape, its calculated GI-SAXS curve disagrees with observed GI-SAXS curve in the Q_Z direction, even when the calculated GI-SAXS curve agrees well with the observed GI-SAXS curve in the Q_Y direction. On the other hand, the calculated GI-SAXS curves for both Q_Y and Q_Z directions agree well with the observed GI-SAXS curves by assuming each of the pores has an ellipsoidal shape. Therefore, the ellipsoidal model is a good approximation for the shape of the pores. Values of the optimized average diameter D and its standard deviation ΔD measured along the direction parallel to the surface are 4.82 nm and 1.54 nm, respectively. The optimized average diameter D_Z and standard deviation ΔD_Z measured along the direction normal to the surface are 3.90 nm and 1.25 nm, respectively. These results indicate that the the nanopores have an ellipsoidal shape with ellipticity of 0.19.

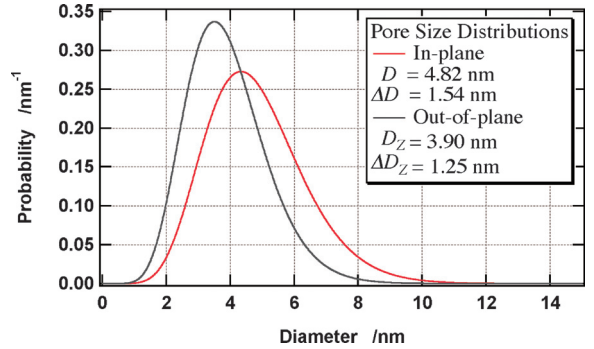

Fig. 8. Pore-size distributions of the porous low-k film.

4.2. Diameter distribution of GaP nano-wire

Recently, semiconductor nanowires and nanotubes with one-dimensional nanostructures have attracted many attentions. A GaP nanowire has been used as a light-emitting device. Optical properties, e.g. peak luminescence wavelength and luminescent efficiency, of an one-dimensional GaP nanowire differ from those of the bulk crystal. It is also reported that the optical properties of a nanowire depends on the diameter of the nanowire. Therefore, the determination of the average diameter and the size distribution of a nanowire is considered to be important for the understanding of the relationship between its diameter and its optical properties. Electron microscope observation techniques are widely used to determine the diameter and the size distribution. However, most of the nanowires have high aspect ratios, such as their diameters and lengths are several dozen nanometers and several dozen micrometers, respectively. Therefore, electron microscopy techniques are not suitable to be used for the determination of the average diameter and the size distribution in a nanowire. On the other hand, the GI-SAXS technique can be used more effectively for the determination of the average diameter and the size distribution.

GI-SAXS measurement for a GaP nanowire, which was perpendicularly-grown on a silicon substrate with catalytic gold nanoparticles, was performed using a Rigaku SuperLab diffractometer (Fig. 3) with a rotating anode X-ray generator operated at 40 kV and 30 mA, and Cu Kα (λ=0.154178 nm) radiation was used. Only the GI-SAXS curve measured along the Q_Y direction was collected by scanning the 2θ axis with an X-ray incidence angle of 0.15°. GI-SAXS for the Q_Z direction was not performed, because the length of the nanowire is too long to be determined by X-ray technique.

In the GI-SAXS analysis, Eq. (7) is used for the scattering cross section of the nanowire assuming that the nanowire is distributed randomly on the substrate. Cylindrical model standing on the substrate was selected as the shape model of the nanowire. Form factor for the standing cylindrical shape can be written as:

$$F(\boldsymbol{Q};D,L)=\frac{2\pi D}{Q'Q_Z}\sin\left(\frac{Q_Z L}{2}\right)J_1\left(\frac{Q'D}{2}\right)e^{i\frac{Q_Z L}{2}} \qquad (18)$$

$$Q'=\sqrt{Q_X^2+Q_Y^2}$$

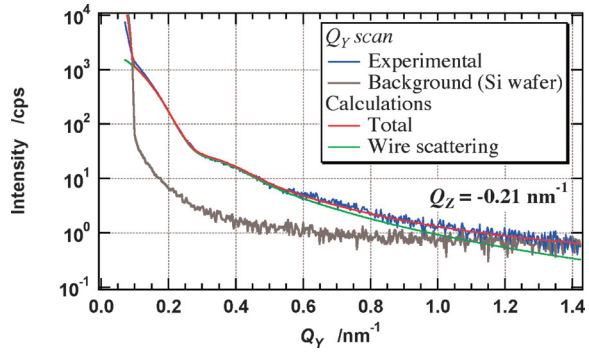

Fig. 9. GI-SAXS curves measured along the Q_Y direction for the GaP nanowire.

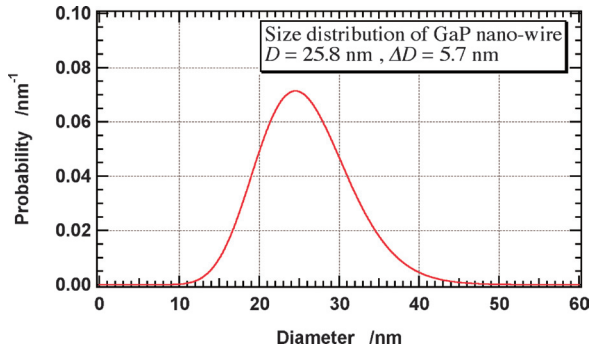

Fig. 10. The size distribution curve for the GaP nanowire.

where D is diameter of the nanowire, L length of the nanowire, and $J_1(x)$ the first-order Bessel function. The observed and calculated GI-SAXS curves and the final the diameter size distribution by using the optimized parameters are shown in Figs. 9 and 10. In this analysis, the length of the nanowire was fixed at 5 μm, because the GI-SAXS curve was collected with Q_Z to be constant, and the length of the nanowire has very little influence on the determination of the diameter. This is evident from Eq. (18). The optimized average diameter D and its standard deviation ΔD of the nanowire are found to be 25.8 nm and 5.7 nm, respectively.

5. Summary

In the past ten years, micro-focused X-ray generators and optics have made a significant progress to meet the rapid advances in nanotechnologies. GI-SAXS is now performed not only at synchrotron radiation facilities but also in conventional laboratories. Successful in-house GI-SAXS results on the characterization of the inner/outer diameter of carbon nanotubes, two-dimensional shape of nanodots, etc. were previously reported.[8]

Recently, high-resolution GI-SAXS has also attracted considerable interests in critical-dimension (CD) measurements of the pitch width for an one-dimensional grating standard in the nanometric lateral scale, in which the pitch width larger than 100 nm is conventional calibrated by optical diffraction with wavelength of 193 nm (DUV laser: Deep ultra violet laser).[9] With the advances of the nanotechnology, miniaturization of the pitch width will be expected to be less than 100 nm. A nano-size pitch width can be difficult to be measured by DUV laser diffraction because of in the Bragg condition. Therefore, GI-SAXS technique is expected to serve as one of the alternatives to optical diffraction technique. Rigaku SuperLab can be used not only for high-resolution GI-XRD (in-plane XRD) analysis, but also for high-resolution GI-SAXS (Bonse-Hart GI-SAXS). Therefore, in-house GI-SAXS will be expected to play an important role in the CD measurements.

References

(1) M. Rauscher, R. Paniago, H. Metzeger, Z. Kovats, J. Domke, H.-D. Pfannes, J. Schulze, and I. Eisele: *J. Appl. Phys.*, **86** (1999), 6763–6769.
(2) D. Badonneau, F. Petroff, J.-L. Maurice, F. Fettar, A. Vaures, and A. Naudon: *Appl. Phys. Lett.*, **76** (2000), 2892–2894.
(3) L. Jiang, Z. Al-Mosheky, and N. Grupid: *Powder Diffraction*, **17** (2002), 81–93.
(4) S. K. Sinha, E. B. Shirota, S. Garoff, and H. B. Stanley: *Phys. Rev. B*, **38** (1988), 2297–2311.
(5) K. Omote, Y. Ito, and S. Kawamura: *Appl. Phys. Lett.*, **82** (2003), 544–546.
(6) L. G. Parratt: *Phys. Rev.*, **95** (1954), 359–369.
(7) L. Lazzari: *J. Appl. Cryst.*, **35** (2002), 406–421.
(8) Y. Ito, K. Inaba, and K. Omote: *J. Phys.*: *Conference Series*, **83** (2007), 012015.
(9) Y. Ito, K. Inaba, K. Omote, Y. Wada, and S. Ikeda: *Jpn. J. Appl. Phys.*, **46** (2007), L773–L775.